

# Majorana finite frequency nonequilibrium quantum noise

Sergey Smirnov

*P. N. Lebedev Physical Institute of the Russian Academy of Sciences, 119991 Moscow, Russia\**

(Dated: April 30, 2019)

Quantum finite frequency noise is one of fundamental aspects in quantum measurements performed during quantum information processing where currently Majorana bound states offer an efficient way to implement fault-tolerant quantum computation via topological protection from decoherence or unitary errors. Thus a detailed exploration of Majorana finite frequency noise spectra, preferably in a nonequilibrium device, is a timely challenge of fundamental importance. Here we present results on finite frequency differential noise that is the derivative of the noise with respect to the frequency. This quantity has universal units of  $e^2$  and scans in high detail all peculiarities of the Majorana noise clearly demonstrating its universal finite frequency features. In particular, we provide photon absorption spectra on all energy scales and reveal a rich structure including universal Majorana plateaus as well as universal Majorana resonances and antiresonances at characteristic frequencies. Our results are of immediate interest to state-of-the-art experiments involving quantum noise mesoscopic detectors able to separately measure photon absorption and emission spectra.

## I. INTRODUCTION

Majorana bound states in condensed matter setups [1] attract at present a lot of attention from a fundamental point of view because they partly mimic Majorana fermions [2] in the elementary particle physics. The topological superconducting phase of the Kitaev model [1] in realistic setups [3–6] provides Majorana bound states localized at the ends of a one-dimensional system. There is a rather high degree of evidence that Majorana bound states have been observed in transport experiments [7–9] measuring the differential conductance. Nevertheless, fully conclusive experiments have still to be performed. For example, thermodynamic experiments able to detect Majorana tunneling entropy [10] do not require any braiding operation and at the same time are fully conclusive with respect to the presence of Majorana bound states. Recent experimental progress in direct entropy measurements [11] within a mesoscopic setup clearly demonstrates that such thermodynamic detections of Majorana bound states are quite feasible and might appear soon.

Practically, non-Abelian Majorana zero-energy modes provide a platform for topological quantum computation [12] as a sequence of unitary transformations implementing braid operations. Since these unitary evolutions depend only on the topological properties of the resulting braids, they are immune to local perturbations. This protects, *e.g.*, quantum storage devices from decoherence errors induced by certain interactions with an environment [13]. Possible experiments on braiding Majorana zero modes have been theoretically proposed in setups with  $T$ -junctions [14, 15]. Braiding schemes avoiding unitary evolutions and using instead a projective measurement are also available via, *e.g.*, an electron teleportation [16].

Noise plays a twofold role in Majorana topological computations. First, although braids are topologically protected, qubits may lose their coherence when Majorana bound states move during a braiding operation in the presence of noise induced by an environment [17]. Second, qubit readout schemes often involve electric currents [16, 18] whose noise governed by Majorana degrees of freedom is in general finite at all frequencies. This finite frequency noise is able to encode the Majorana qubit state for a readout by a proper quantum noise detector able to reach the quantum limit [19]. Moreover, noise itself may be viewed as a unique Majorana signature extracted from advanced transport experiments alternative to the differential conductance.

Majority of research on Majorana noise in mesoscopic setups is focused on symmetrized noise [20–23] which is often explored in the static limit, *i.e.* at zero frequency. A characteristic feature of zero frequency nonequilibrium Majorana noise is its universal behavior leading, *e.g.*, to universal effective charges [24] equal to  $e/2$  and  $3e/2$  at low and high bias voltages, respectively, or to universal ratios between nonlinear response coefficients of Majorana thermoelectric noise and mean current [25].

In contrast to the static limit, quantum noise at finite frequencies in Majorana setups is not so well investigated, especially in quantum dot setups, such as, *e.g.*, the one shown in Fig. 1, which admit a gate tuning and may be used for simple tests of universal Majorana signatures. For example, in topological superconductor-normal metal structures [26, 27] finite frequency noise induced by Majorana zero modes has been investigated. However, universal fingerprints of the Majorana finite frequency quantum noise have never been discussed. Moreover, previously published results study noise itself and not differential noise which is better (see below) suited to explore universal nature of Majorana finite frequency noise. While the symmetrized finite frequency noise may be interpreted as a classical stochastic force, the nonsymmetrized, or quantum, finite-frequency noise admits interpretation [19] in terms of photon absorption and emis-

\* 1) sergej.physik@gmail.com

2) sergey.smirnov@physik.uni-regensburg.de

3) ssmirnov@sci.lebedev.ru

sion processes (shown schematically in Fig. 1 by, respectively, red and blue wavy arrows). However, in systems, where one can reach the quantum limit in a realistic experiment, photon absorption/emission spectra, induced by Majorana zero modes, remain unexplored.

Here, we focus on the differential quantum noise which is the derivative of the quantum noise with respect to the frequency. This quantity has two advantages in comparison with the quantum noise itself. First, the differential quantum noise has universal units of  $e^2$ . Thus this quantity is a natural tool to characterize universal features in Majorana finite frequency quantum noise. Second, the differential quantum noise allows one to reveal in high detail specific behavior of the quantum noise including possible fine structures which one might easily skip when observing behavior of the quantum noise itself. In particular, we analyze the photon absorption spectra at all energy scales and reveal several remarkable properties of the differential quantum noise as a function of the frequency  $\nu$  ( $h\nu = \hbar\omega$ ) at very low temperatures  $T$  (the lowest energy scale) and various bias voltages  $V$ . We find that at low bias voltages 1) it has two universal plateaus,  $7e^2/4$  and  $2e^2$ ; 2) at  $h\nu = |eV|/2$  there is a very narrow antiresonance with the full width at half of its minimum equal to  $4k_B T$ ; 3) at  $h\nu = 2|\eta|$  there is a resonance with full width at half of its maximum equal to  $\Gamma$ ; at large bias voltages 4) the antiresonance located at  $h\nu = |eV|/2$  turns into a resonance with the universal maximum  $e^2/2$  and the full width at half of the maximum equal to  $\Gamma$ ; 5) at  $h\nu = 2|\eta| \mp |eV|/2$  there develop two new resonances with the universal maximum  $e^2$  and the full width at half of the maximum equal to  $\Gamma/2$ ; 6) the resonance located at  $h\nu = 2|\eta|$  turns into an antiresonance-resonance pair in which the full widths of the antiresonance and resonance at half of the minimum and maximum, respectively, are both equal to  $\Gamma$ ; 7) at all other frequencies the differential quantum noise vanishes.

The paper is organized as follows. In Section II we describe a physical setup which can be implemented in realistic experiments. The results obtained for quantum finite frequency noise spectra are presented in Section III. With Section IV we conclude the paper.

## II. PHYSICAL MODEL

In this paper we present results for finite frequency quantum noise induced by Majorana zero modes in the physical setup shown in Fig. 1. The system in this setup represents a quantum dot which is coupled to two massive normal metals playing the role of the left and right contacts. The setup also involves a grounded topological superconductor implementing the topological phase of the Kitaev's model with two Majorana bound states at its ends one of which is coupled to the quantum dot. As a result, the quantum dot states are entangled with the Majorana degrees of freedom. When a bias voltage is applied to the normal metals, electric current flows through

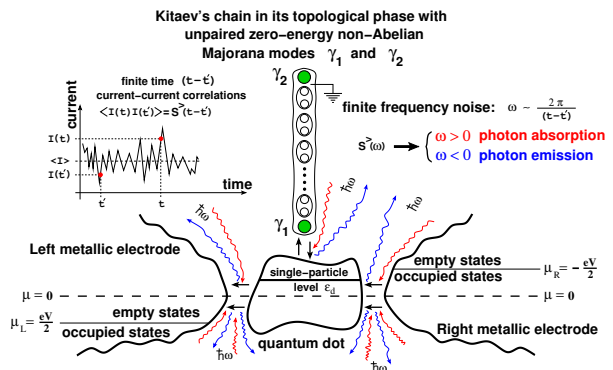


FIG. 1. A schematic illustration of a conceivable experimental setup. Quantum transport through a quantum dot is implemented via tunneling processes of two kinds: 1) tunneling of strength  $\Gamma$  between the quantum dot and normal metallic electrodes (left (L) and right (R) contacts); 2) tunneling of strength  $|\eta|$  between the quantum dot and a topological superconductor implementing the Kitaev's chain with two Majorana bound states at its ends. Energetically both kinds of tunneling admit photon absorption and emission processes. One may access the photon absorption/emission spectra via the greater noise measured, *e.g.*, in the left contact,  $S^>(t-t') = \langle I_L(t)I_L(t') \rangle$ . The values of the electric current,  $I(t)$  and  $I(t')$ , observed, respectively, at instants of time  $t$  and  $t'$ , are correlated. Correlations at finite time intervals,  $0 < |t-t'| < \infty$ , lead to noise  $S^>(\omega)$  at finite frequencies  $\omega$  providing absorption,  $\omega > 0$ , and emission,  $\omega < 0$ , spectra. Characteristic photon frequencies,  $\omega_c$ , are determined by the tunneling couplings,  $\omega_c \sim \Gamma/\hbar$ ,  $|\eta|/\hbar$ . Applying a bias voltage  $V$  to the contacts, one disturbs the system from equilibrium. The nonequilibrium noise is enriched by a new characteristic frequency,  $\omega_c \sim |eV|/\hbar$ .

this Majorana quantum dot system and carries Majorana signatures both in its mean value and its fluctuations. To understand the impact of the Majorana bound states on fluctuations of the electric current, below we describe this setup more precisely by specifying its full Hamiltonian which is the sum of the Hamiltonians of the quantum dot, contacts, topological superconductor as well as the Hamiltonians describing the interactions of the quantum dot with the contacts and topological superconductor.

The quantum dot with one nondegenerate single-particle level  $\epsilon_d$  is described by the noninteracting Hamiltonian

$$\hat{H}_d = \epsilon_d d^\dagger d. \quad (1)$$

A gate voltage may shift  $\epsilon_d$  relative to the chemical potential  $\mu$ . The left and right contacts are normal metals with continuous energy spectra  $\epsilon_k$  characterized by a constant density of states  $\nu_c/2$ . Their Hamiltonian is

$$\hat{H}_c = \sum_{l=L,R} \sum_k \epsilon_k c_{lk}^\dagger c_{lk}. \quad (2)$$

They are in an equilibrium state characterized by temperature  $T$ . An external bias voltage  $V$  may be applied to the contacts setting their chemical potentials as

$\mu_{L,R} = \pm eV/2$  (see Fig. 1 for  $eV < 0$ ). The low-energy sector of the topological superconductor is modeled by

$$\hat{H}_{tsc} = i\xi\gamma_2\gamma_1/2, \quad (3)$$

where  $\gamma_{1,2}$  are the Majorana operators such that  $\gamma_{1,2}^\dagger = \gamma_{1,2}$ . The anticommutation relations  $\{\gamma_i, \gamma_j\} = 2\delta_{ij}$  establish the algebraic structure known as the Clifford algebra. In general Majorana bound states have a finite spatial overlap which we take into account via the overlap energy  $\xi$ . The quantum dot interacts via tunneling (shown in Fig. 1 by black arrows) with the contacts,

$$\hat{H}_{d-c} = \sum_{l=L,R} \sum_k \mathcal{T}c_{lk}^\dagger d + \text{H.c.}, \quad (4)$$

and the topological superconductor,

$$\hat{H}_{d-tsc} = \eta^* d^\dagger \gamma_1 + \text{H.c.} \quad (5)$$

The corresponding tunneling strengths are  $\Gamma = 2\pi\nu_c|\mathcal{T}|^2$  and  $|\eta|$ .

To explore the quantum noise in a general nonequilibrium setup it is convenient to employ the Keldysh generating functional [28],

$$\begin{aligned} Z[J_l(t)] &= \int \mathcal{D}[\bar{\theta}(t), \theta(t)] e^{\frac{i}{\hbar} S_K[\bar{\theta}(t), \theta(t); J_l(t)]}, \\ \mathcal{D}[\bar{\theta}(t), \theta(t)] &= \\ &= \mathcal{D}[\bar{\psi}(t), \psi(t)] \mathcal{D}[\bar{\phi}_{lk}(t), \phi_{lk}(t)] \mathcal{D}[\bar{\zeta}(t), \zeta(t)], \end{aligned} \quad (6)$$

where  $S_K[\bar{\theta}(t), \theta(t); J_l(t)]$  is the total Keldysh action with the Grassmann fields of the quantum dot ( $\bar{\psi}(t), \psi(t)$ ), contacts ( $\bar{\phi}_{lk}(t), \phi_{lk}(t)$ ) and the topological superconductor ( $\bar{\zeta}(t), \zeta(t)$ ) defined on the Keldysh closed time contour,  $t \in \mathcal{C}_K$ . For  $S_K[\bar{\theta}(t), \theta(t); J_l(t)]$  one has the sum,

$$\begin{aligned} S_K[\bar{\theta}(t), \theta(t); J_l(t)] &= \\ &= S_d[\bar{\psi}(t), \psi(t)] + S_c[\bar{\phi}_{lk}(t), \phi_{lk}(t)] + \\ &+ S_{tsc}[\bar{\zeta}(t), \zeta(t)] + S_{d-c}[\bar{\psi}(t), \psi(t); \bar{\phi}_{lk}(t), \phi_{lk}(t)] + \\ &+ S_{d-tsc}[\bar{\psi}(t), \psi(t); \bar{\zeta}(t), \zeta(t)] + \\ &+ S_{scr}[\bar{\psi}(t), \psi(t); \bar{\phi}_{lk}(t), \phi_{lk}(t); J_l(t)], \end{aligned} \quad (7)$$

of the Keldysh actions describing the quantum dot,  $S_d$ , contacts,  $S_c$ , topological superconductor,  $S_{tsc}$ , tunneling between the quantum dot and contacts,  $S_{d-c}$ , tunneling between the quantum dot and topological superconductor,  $S_{d-tsc}$ , and the source action  $S_{scr}$ .

As usual, the Keldysh actions  $S_d$ ,  $S_c$  and  $S_{tsc}$  are represented in the retarded-advanced space by upper triangular  $2 \times 2$  matrices whose upper/lower diagonal elements are the corresponding inverse retarded/advanced Green's functions and the upper off-diagonal elements are related to the corresponding Fermi-Dirac distribution functions  $f$  as  $i\delta(1-2f)$ ,  $\delta \rightarrow 0^+$ .

The tunneling actions,

$$\begin{aligned} S_{d-c}[\bar{\psi}(t), \psi(t); \bar{\phi}_{lk}(t), \phi_{lk}(t)] &= \\ &= - \int_{-\infty}^{\infty} dt \sum_{l=L,R} \sum_k \{ \mathcal{T}[\bar{\phi}_{lk+}(t)\psi_+(t) - \\ &- \bar{\phi}_{lk-}(t)\psi_-(t)] + \\ &+ \mathcal{T}^*[\bar{\psi}_+(t)\phi_{lk+}(t) - \bar{\psi}_-(t)\phi_{lk-}(t)] \}, \end{aligned} \quad (8)$$

$$\begin{aligned} S_{d-tsc}[\bar{\psi}(t), \psi(t); \bar{\zeta}(t), \zeta(t)] &= \\ &= - \int_{-\infty}^{\infty} dt \{ \eta^*[\bar{\psi}_+(t)\zeta_+(t) + \bar{\psi}_+(t)\bar{\zeta}_+(t) - \\ &- \bar{\psi}_-(t)\zeta_-(t) - \bar{\psi}_-(t)\bar{\zeta}_-(t)] + \\ &+ \eta[\bar{\zeta}_+(t)\psi_+(t) + \zeta_+(t)\psi_+(t) - \\ &- \bar{\zeta}_-(t)\psi_-(t) - \zeta_-(t)\psi_-(t)] \}, \end{aligned} \quad (9)$$

written on the forward/backward (subindex  $+/-$ ) branches of  $\mathcal{C}_K$ , take into account the interactions between the quantum dot and contacts, Eq. (8), as well as between the quantum dot and topological superconductor, Eq. (9). Here the Grassmann fields  $\zeta_{\pm}(t)$  and  $\bar{\zeta}_{\pm}(t)$  correspond to the complex Dirac fermion representation of the Majorana operators. This representation clearly shows how superconductivity appears in the formalism involving the anomalous terms in Eq. (9),  $\bar{\psi}_{\pm}(t)\bar{\zeta}_{\pm}(t)$  and  $\zeta_{\pm}(t)\psi_{\pm}(t)$ , which lead, as discussed below, to anomalous contributions to the quantum noise. Note, that these anomalous contributions result exclusively from the presence of the topological superconductor: they could not have appeared if one had replaced the topological superconductor with a normal system, *e.g.*, with another normal quantum dot.

Current-current correlators may be obtained via proper differentiation of  $Z[J_l(t)]$  with respect to the source field  $J_l(t)$  coupled to the electric current in the source action,

$$\begin{aligned} S_{scr} &= - \int_{-\infty}^{\infty} dt \sum_{l=L,R} \sum_{q=+,-} J_{lq}(t) I_{lq}(t), \\ I_{lq}(t) &= \frac{ie}{\hbar} \sum_k [\mathcal{T}\bar{\phi}_{lkq}(t)\psi_q(t) - \mathcal{T}^*\bar{\psi}_q(t)\phi_{lkq}(t)], \end{aligned} \quad (10)$$

where the subscript  $q$  denotes the forward ( $q = +$ ) and backward ( $q = -$ ) branches of  $\mathcal{C}_K$ . In particular, for the correlations between the values of the electric current in contacts  $l$  and  $l'$  taken at instants of time  $t$  and  $t'$ ,  $I_l(t)$  and  $I_{l'}(t')$ , one obtains

$$\begin{aligned} \langle I_l(t) I_{l'}(t') \rangle &\equiv \langle I_{l-}(t) I_{l'+}(t') \rangle_{S_K} = \\ &= (i\hbar)^2 \frac{\delta^2 Z[J_l(t)]}{\delta J_{l-}(t) \delta J_{l'+}(t')} \Big|_{J_{lq}(t)=0}, \end{aligned} \quad (11)$$

where  $\langle \dots \rangle_{S_K}$  is the functional averaging with respect to the total Keldysh action at vanishing sources,

$$\begin{aligned} \langle \mathcal{F}[\bar{\theta}(t), \theta(t)] \rangle_{S_K} &\equiv \\ &\equiv \int \mathcal{D}[\bar{\theta}(\tilde{t}), \theta(\tilde{t})] e^{\frac{i}{\hbar} S_K[\bar{\theta}(\tilde{t}), \theta(\tilde{t})]} \mathcal{F}[\bar{\theta}(t), \theta(t)], \end{aligned} \quad (12)$$

$$\begin{aligned}
S_K[\bar{\theta}(t), \theta(t)] &\equiv S_K[\bar{\theta}(t), \theta(t); J_l(t) = 0] = \\
&= S_d[\bar{\psi}(t), \psi(t)] + S_c[\bar{\phi}_{lk}(t), \phi_{lk}(t)] + \\
&+ S_{tsc}[\bar{\zeta}(t), \zeta(t)] + S_{d-c}[\bar{\psi}(t), \psi(t); \bar{\phi}_{lk}(t), \phi_{lk}(t)] + \\
&+ S_{d-tsc}[\bar{\psi}(t), \psi(t); \bar{\zeta}(t), \zeta(t)].
\end{aligned} \tag{13}$$

Integrating first out the contacts Grassmann fields and afterwards taking the second derivative in Eq. (11) it is

easy to see that the current-current correlator is the sum,

$$\langle I_l(t) I_{l'}(t') \rangle = S_{1_{ll'}}(t, t') + S_{2_{ll'}}(t, t'), \tag{14}$$

of a one-particle term  $S_{1_{ll'}}(t, t')$  and also a two-particle term  $S_{2_{ll'}}(t, t')$ .

Restoring the field integrals over the contacts Grassmann fields one can express the terms  $S_{1_{ll'}}(t, t')$  and  $S_{2_{ll'}}(t, t')$  using the functional averaging defined in Eqs. (12) and (13),

$$\begin{aligned}
S_{1_{ll'}}(t, t') &= \delta_{ll'} |\mathcal{T}|^2 (-i) \left( \frac{e}{2\hbar} \right)^2 \sum_k \left\{ \langle [\psi_1(t') + \psi_2(t')] [-\bar{\psi}_1(t) + \bar{\psi}_2(t)] \rangle_{S_K} [G_{lk}^R(t-t') + G_{lk}^K(t-t') - \right. \\
&- G_{lk}^A(t-t')] + \langle [\psi_1(t) - \psi_2(t)] [\bar{\psi}_1(t') + \bar{\psi}_2(t')] \rangle_{S_K} [-G_{lk}^R(t'-t) + G_{lk}^K(t'-t) + G_{lk}^A(t'-t)] \left. \right\},
\end{aligned} \tag{15}$$

$$\begin{aligned}
S_{2_{ll'}}(t, t') &= |\mathcal{T}|^4 \frac{(-1)}{\hbar^2} \left( \frac{e}{2\hbar} \right)^2 \int_{-\infty}^{\infty} dt_1 \int_{-\infty}^{\infty} dt_2 \sum_{k_1, k_2} \left\langle \left\{ [-\psi_1(t) + \psi_2(t)] [\bar{\psi}_1(t_2) G_{lk_2}^R(t_2-t) - \right. \right. \\
&- \bar{\psi}_1(t_2) G_{lk_2}^K(t_2-t) - \bar{\psi}_2(t_2) G_{lk_2}^A(t_2-t)] - [G_{lk_2}^R(t-t_2) \psi_1(t_2) + G_{lk_2}^K(t-t_2) \psi_2(t_2) - \\
&- G_{lk_2}^A(t-t_2) \psi_2(t_2)] [-\bar{\psi}_1(t) + \bar{\psi}_2(t)] \left. \right\} \left\{ [\psi_1(t') + \psi_2(t')] [\bar{\psi}_1(t_1) G_{l'k_1}^R(t_1-t') + \bar{\psi}_1(t_1) G_{l'k_1}^K(t_1-t') + \right. \\
&+ \bar{\psi}_2(t_1) G_{l'k_1}^A(t_1-t')] - [G_{l'k_1}^R(t'-t_1) \psi_1(t_1) + G_{l'k_1}^K(t'-t_1) \psi_2(t_1) + \\
&+ G_{l'k_1}^A(t'-t_1) \psi_2(t_1)] [\bar{\psi}_1(t') + \bar{\psi}_2(t')] \left. \right\} \right\rangle_{S_K},
\end{aligned} \tag{16}$$

where the Keldysh rotation,

$$\psi_q(t) = \frac{1}{\sqrt{2}} [\psi_1(t) + q\psi_2(t)], \quad \bar{\psi}_q(t) = \frac{1}{\sqrt{2}} [\bar{\psi}_2(t) + q\bar{\psi}_1(t)], \tag{17}$$

has been used and  $G_{lk}^{R,A,K}(t-t')$  are the conventional contacts retarded, advanced and Keldysh Green's functions, respectively.

The one-particle contribution in Eq. (15) involves averages of products of only two Grassmann fields of the quantum dot. This contribution contains only normal terms,  $\langle \psi_r(t) \bar{\psi}_{r'}(t') \rangle_{S_K}$ , ( $r, r' = 1, 2$ ). Obviously, the anomalous terms,  $\langle \psi_r(t) \psi_{r'}(t') \rangle_{S_K}$  or  $\langle \bar{\psi}_r(t) \bar{\psi}_{r'}(t') \rangle_{S_K}$ , cannot appear in  $S_{1_{ll'}}(t, t')$ .

The anomalous terms definitely arise when one averages products of four Grassmann fields in the two-particle contribution, Eq. (16). Since the total Keldysh action in Eq. (13) is quadratic, the average of a product of four Grassmann fields can be written as a sum of products of the averages of two Grassmann fields according to Wick's theorem. In particular,

$$\begin{aligned}
\langle \psi_{r_1}^1 \bar{\psi}_{r_2}^2 \psi_{r_3}^3 \bar{\psi}_{r_4}^4 \rangle_{S_K} &= \langle \psi_{r_1}^1 \bar{\psi}_{r_2}^2 \rangle_{S_K} \langle \psi_{r_3}^3 \bar{\psi}_{r_4}^4 \rangle_{S_K} - \\
&- \langle \psi_{r_1}^1 \bar{\psi}_{r_4}^4 \rangle_{S_K} \langle \psi_{r_3}^3 \bar{\psi}_{r_2}^2 \rangle_{S_K} - \langle \psi_{r_1}^1 \psi_{r_3}^3 \rangle_{S_K} \langle \bar{\psi}_{r_2}^2 \bar{\psi}_{r_4}^4 \rangle_{S_K}.
\end{aligned} \tag{18}$$

In Eq. (18)  $\psi_{r_1}^1, \bar{\psi}_{r_2}^2, \psi_{r_3}^3, \bar{\psi}_{r_4}^4$  ( $r_{1,2,3,4} = 1, 2$ ) schematically denote four Grassmann fields in a particular contribution resulting from a product of four square brackets in the integrand of (16). The superscript enumerates,

from left to right, those four square brackets from which the corresponding Grassmann fields are taken to form the particular product (18). The subscript provides the corresponding component of the retarded-advanced space.

All those terms in Eq. (16) which correspond to the third term in the right hand side of Eq. (18) give the anomalous two-particle contributions to  $\langle I_l(t) I_{l'}(t') \rangle$ . We emphasize once again that the appearance of these anomalous contributions in the mathematical formalism is a direct consequence of superconductivity present in the physical system. The anomalous contributions would have never appeared if one had replaced the topological superconductor with, *e.g.*, another normal quantum dot.

Let us introduce a "particle-hole" space via the Grassmann fields  $\psi_{ar}$  ( $a = p, h; r = 1, 2$ ),

$$\begin{aligned}
\psi_{ar}(t) &\equiv \bar{\psi}_r(t), \quad a = p, \\
\psi_{ar}(t) &\equiv \psi_r(t), \quad a = h.
\end{aligned} \tag{19}$$

Then the averages in Eq. (15) as well as the averages appearing in Eq. (16) via Eq. (18) are expressed in

terms of the hole-particle, hole-hole and particle-particle

retarded, advanced and Keldysh Green's functions of the quantum dot:

$$\langle \psi_{hr}(t) \psi_{pr'}(t') \rangle_{S_K} = \begin{pmatrix} i \mathcal{G}_{hp}^R(t-t') & i \mathcal{G}_{hp}^K(t-t') \\ 0 & i \mathcal{G}_{hp}^A(t-t') \end{pmatrix}, \quad (20)$$

$$\langle \psi_{hs}(t) \psi_{hs'}(t') \rangle_{S_K} = \begin{pmatrix} i \mathcal{G}_{hh}^K(t-t') & i \mathcal{G}_{hh}^R(t-t') \\ i \mathcal{G}_{hh}^A(t-t') & 0 \end{pmatrix}, \quad (21)$$

$$\langle \psi_{ps}(t) \psi_{ps'}(t') \rangle_{S_K} = \begin{pmatrix} 0 & i \mathcal{G}_{pp}^A(t-t') \\ i \mathcal{G}_{pp}^R(t-t') & i \mathcal{G}_{pp}^K(t-t') \end{pmatrix}. \quad (22)$$

The total Keldysh action, Eq. (13), is quadratic and thus the quantum dot Green's functions are the elements of the inverse kernel of the effective Keldysh action obtained from the total Keldysh action after integrating out the Grassmann fields of the contacts and topological su-

perconductor. Although the effective Keldysh action is nonlocal in time, one can transform to the frequency domain and easily find the expressions for the hole-particle, hole-hole and particle-particle retarded, advanced [10] and Keldysh [25] Green's functions of the quantum dot:

$$\begin{aligned} \mathcal{G}_{hp}^R(\epsilon) &= \frac{N_{hp}^R(\epsilon)}{f(\epsilon)}, & \mathcal{G}_{hh}^R(\epsilon) &= \frac{-8\hbar(\eta^*)^2\epsilon}{f(\epsilon)}, & \mathcal{G}_{pp}^R(\epsilon) &= \frac{-8\hbar\eta^2\epsilon}{f(\epsilon)}, \\ \mathcal{G}_{hp}^A(\epsilon) &= [\mathcal{G}_{hp}^R(\epsilon)]^*, & \mathcal{G}_{hh}^A(\epsilon) &= [\mathcal{G}_{hh}^R(\epsilon)]^*, & \mathcal{G}_{pp}^A(\epsilon) &= [\mathcal{G}_{pp}^R(\epsilon)]^*, \\ f(\epsilon) &= 4\epsilon^4 - \epsilon^2(\Gamma^2 + 4\epsilon_d^2 + 4\xi^2 + 16|\eta|^2) + \xi^2(\Gamma^2 + 4\epsilon_d^2) + i4\Gamma[\epsilon^3 - \epsilon(\xi^2 + 2|\eta|^2)], \\ N_{hp}^R(\epsilon) &= 2\hbar\{-4|\eta|^2\epsilon - (\xi^2 - \epsilon^2)[i\Gamma + 2(\epsilon_d + \epsilon)]\}, \end{aligned} \quad (23)$$

$$\begin{aligned} \mathcal{G}_{hp}^K(\epsilon) &= \frac{N_{hp}^K(\epsilon)}{|f(\epsilon)|^2}, & \mathcal{G}_{hh}^K(\epsilon) &= \frac{N_{hh}^K(\epsilon)}{|f(\epsilon)|^2}, & \mathcal{G}_{pp}^K(\epsilon) &= \frac{N_{pp}^K(\epsilon)}{|f(\epsilon)|^2}, \\ N_{hp}^K(\epsilon) &= -2i\Gamma\hbar\{(F_L(\epsilon) + F_R(\epsilon))(\xi^2 - \epsilon^2)[\Gamma^2 + 4(\epsilon_d + \epsilon)^2] + \\ &+ 16|\eta|^2\epsilon[(F_L(\epsilon) + F_R(\epsilon))(\xi^2 - \epsilon^2)(\epsilon_d + \epsilon) + |\eta|^2\epsilon(F_L(\epsilon) - F_L(-\epsilon) + F_R(\epsilon) - F_R(-\epsilon))]\}, \\ N_{hh}^K(\epsilon) &= 8\Gamma\hbar(\eta^*)^2\epsilon\{(\xi^2 - \epsilon^2)[(F_L(\epsilon) + F_L(-\epsilon) + F_R(\epsilon) + F_R(-\epsilon))(\Gamma - 2i\epsilon_d) + \\ &+ 2i\epsilon(F_L(-\epsilon) - F_L(\epsilon) + F_R(-\epsilon) - F_R(\epsilon))] + 4i|\eta|^2\epsilon(F_L(-\epsilon) - F_L(\epsilon) + F_R(-\epsilon) - F_R(\epsilon))\}, \\ N_{pp}^K(\epsilon) &= -(N_{hh}^K(\epsilon))^*, \end{aligned} \quad (24)$$

where  $F_{L,R}(\epsilon)$  are defined through the Fermi-Dirac distributions  $f_{L,R}(\epsilon)$  of, respectively, the left and right contacts as  $F_{L,R}(\epsilon) \equiv 1 - 2f_{L,R}(\epsilon)$ .

Below we use Eqs. (15), (16), (18) and (20)-(24) as a complete set of expressions to obtain the Fourier transform of  $\langle I_L(t)I_L(t') \rangle$  via numerical integrations. We perform these numerical integrations in the frequency domain in order to make use of Eqs. (23) and (24).

To be more precise, we investigate the greater current-current correlator in the left contact,

$$S^>(t-t'; V) = \langle I_L(t)I_L(t') \rangle - I_L^2(V), \quad (25)$$

where  $I_L(V)$  is the corresponding mean current. The Fourier transform

$$S^>(\omega, V) = \int_{-\infty}^{\infty} dt e^{i\omega t} S^>(t, V), \quad (26)$$

provides the photon absorption/emission spectra  $S^{ab/em}$ ,

$$S^{ab/em}(\omega, V) = \begin{cases} S^>(\omega, V), & \omega > 0 \\ S^<(\omega, V), & \omega < 0 \end{cases}, \quad (27)$$

which are of direct experimental interest.

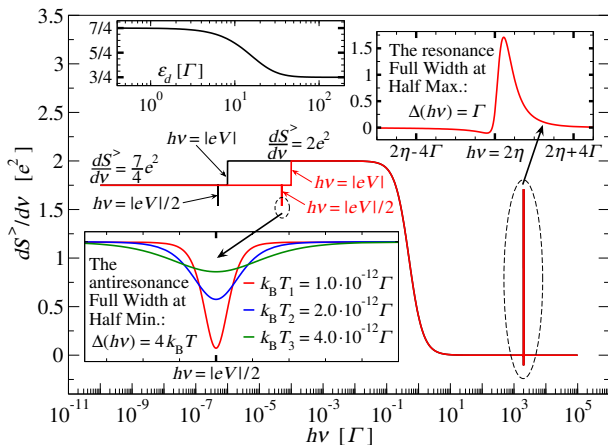


FIG. 2. The differential quantum noise  $\partial S^>(\nu, V)/\partial\nu$  as a function of the frequency  $\nu$  ( $h\nu = \hbar\omega$ ) is shown for the case of very small bias voltages,  $|eV| \ll \Gamma$ . Here  $k_B T/\Gamma = 10^{-12}$ ,  $\epsilon_d/\Gamma = 8.0$ ,  $|\eta|/\Gamma = 10^3$  and  $\xi/\Gamma = 10^{-4}$ . The black and red curves are for  $|eV|/\Gamma = 10^{-6}$  and  $|eV|/\Gamma = 10^{-4}$ , respectively. The lower inset shows the antiresonance whose minimum is located at  $h\nu = |eV|/2$ . The upper left inset shows the dependence of this minimum on  $\epsilon_d$  which may be controlled by a gate voltage. The upper right inset shows the antiresonance-resonance pair, located in the vicinity of  $h\nu = 2|\eta|$ .

To access finite frequency quantum noise induced by Majorana zero modes we explore the transport regime governed by strong Majorana tunneling,

$$|\eta| > \max\{|\epsilon_d|, |eV|, k_B T, \Gamma, \xi\}. \quad (28)$$

We obtain the differential quantum noise  $\partial S^>(\nu, V)/\partial\nu$  ( $h\nu = \hbar\omega$ ) via, first, numerical integrations (using, *e.g.*, Simpson's rule) in the frequency domain, providing  $S^>(\nu, V)$  on a fine frequency grid, and, afterwards, applying finite differences (using, *e.g.*, forward difference or backward difference) to obtain  $\partial S^>(\nu, V)/\partial\nu$ . Due to high precision in the numerical frequency integrations necessary to provide highly precise values of  $S^>(\nu, V)$  to later obtain reliable values of the derivative  $\partial S^>(\nu, V)/\partial\nu$  the numerical computations are very time consuming but still feasible. In particular, below we focus on the photon absorption spectra, *i.e.* on  $\partial S^>(\nu, V)/\partial\nu$  for  $\nu > 0$ .

### III. RESULTS

In Fig. 2 we show the results for the differential quantum noise in the regime  $|eV| \ll \Gamma$ . It reveals a highly detailed structure of the photon absorption ( $\nu > 0$ ) spectrum. For frequencies  $h\nu \ll \Gamma$  the differential noise is represented by two plateaus with universal values  $\partial S^>(\nu, V)/\partial\nu = 7e^2/4$  for  $h\nu < |eV|$  and  $\partial S^>(\nu, V)/\partial\nu = 2e^2$  for  $h\nu > |eV|$ . At  $h\nu = |eV|/2$  the differential noise shows an antiresonance having the full

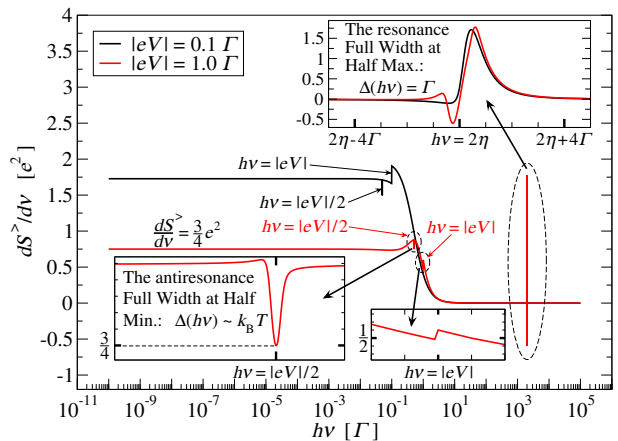


FIG. 3. The differential quantum noise  $\partial S^>(\nu, V)/\partial\nu$  as a function of the frequency  $\nu$  is shown for the case of small and moderate bias voltages. The black and red curves show  $\partial S^>(\nu, V)/\partial\nu$  for  $|eV|/\Gamma = 0.1$  and  $|eV|/\Gamma = 1.0$ , respectively. The other parameters are the same as in Fig. 2. The lower left inset shows the antiresonance which is still present in the case  $|eV|/\Gamma = 1.0$  and has its minimum located at  $h\nu = |eV|/2$ . The lower right inset shows a jump at  $h\nu = |eV|$  for the case  $|eV|/\Gamma = 1.0$ . The upper inset shows for the case  $|eV|/\Gamma = 1.0$  the resonance-antiresonance-resonance trio located in the vicinity of  $h\nu = 2|\eta|$ .

width equal to  $4k_B T$  at half of its minimum, as shown in the lower inset for  $|eV|/\Gamma = 10^{-4}$  and three different temperatures,  $k_B T_1/\Gamma = 10^{-12}$  (red),  $k_B T_2/\Gamma = 2.0 \cdot 10^{-12}$  (blue) and  $k_B T_3/\Gamma = 4.0 \cdot 10^{-12}$  (green). This antiresonance is not universal, *i.e.* it depends on the gate voltage tuning  $\epsilon_d$ . The minimum of the antiresonance as a function of  $\epsilon_d$  is shown in the upper left inset. It has two asymptotics. The minimal value,  $3e^2/4$ , is reached at large values of  $\epsilon_d$  while the maximal value,  $7e^2/4$ , is reached in the limit  $\epsilon_d \rightarrow 0$ . Therefore, the antiresonance disappears when  $\epsilon_d = 0$ . Near  $h\nu = 2|\eta|$  the differential noise exhibits a strong resonance having the full width equal to  $\Gamma$  at half of its maximum as shown in the upper right inset. Just before this strong resonance one also notices a very shallow antiresonance. For the present case of very small bias voltages,  $|eV| \ll \Gamma$ , this antiresonance-resonance pair, located in the vicinity of  $h\nu = 2|\eta|$ , is independent of the bias voltage  $V$ .

In Fig. 3 the photon absorption spectrum is analyzed in the regime  $|eV| \lesssim \Gamma$ , *i.e.*, respectively, for small bias voltages,  $|eV| < \Gamma$ , and moderate bias voltages,  $|eV| \sim \Gamma$ . As one can see, in this regime the differential noise has a plateau at  $h\nu \ll |eV|$ . The value of this plateau is, however, suppressed below its universal maximum  $7e^2/4$  reached in the regime of very small bias voltages,  $|eV| \ll \Gamma$ , for  $h\nu < |eV|$  (see Fig. 2). When  $|eV| = \Gamma$ , the universal value of this plateau is  $3e^2/4$  (red curve). As in the regime  $|eV| \ll \Gamma$ , shown in Fig. 2, also in the present case,  $|eV| \lesssim \Gamma$ , the differential quantum noise has a jump at  $h\nu = |eV|$ . However, now this jump is significantly reduced, as shown in the lower right

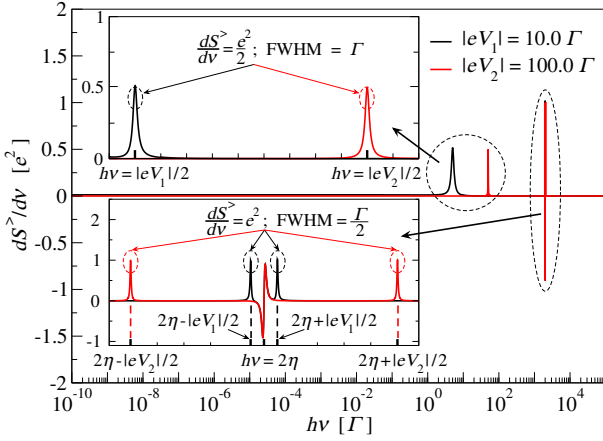


FIG. 4. The differential quantum noise  $\partial S^>(\nu, V)/\partial\nu$  as a function of the frequency  $\nu$  is shown for the case of large and very large bias voltages. The black and red curves show  $\partial S^>(\nu, V)/\partial\nu$  for, respectively,  $V = V_1$  and  $V = V_2$  with  $|eV_1|/\Gamma = 10.0$  and  $|eV_2|/\Gamma = 100.0$ . The other parameters are the same as in Fig. 2. The upper inset shows the resonances at  $h\nu = |eV_1|/2$  (black curve) and  $h\nu = |eV_2|/2$  (red curve). The lower inset shows the antiresonance-resonance pair located in the vicinity of  $h\nu = 2|\eta|$  as well as the resonances located at  $h\nu = 2|\eta| \mp |eV_1|/2$  (black curve) and  $h\nu = 2|\eta| \mp |eV_2|/2$  (red curve).

inset for  $|eV| = \Gamma$ , and, as one can also see, this is a jump in a decreasing function and not a jump separating two universal plateaus of the differential noise as is the case in Fig. 2. At  $h\nu = |eV|/2$  the situation starts to qualitatively change when the bias voltage grows. In particular, when  $|eV| = \Gamma$  (red curve), there develops a wide resonance whose full width is of order  $\Gamma$  at half of its maximum. This wide resonance is split in its very middle, *i.e.* at  $h\nu = |eV|/2$ , by the extremely narrow antiresonance which has already developed in the regime of very small bias voltages,  $|eV| \ll \Gamma$ , as shown in the lower inset of Fig. 2. Here, for the bias voltage  $|eV| = \Gamma$ , the full width of this extremely narrow antiresonance is still of order  $k_B T$  at half of its minimum as shown in the lower left inset. The minimum of this antiresonance is equal to the value of the plateau at  $h\nu \ll |eV|$ , *i.e.* to  $3e^2/4$ , as emphasized by the horizontal dashed line in the lower left inset. In the vicinity of  $h\nu = 2|\eta|$  qualitative changes in the behavior of the differential noise become visible too. As one can see in the upper inset, when  $|eV| = \Gamma$  (red curve), there appears a new resonance just before the antiresonance-resonance pair which has already developed in the regime of very small bias voltages,  $|eV| \ll \Gamma$  as shown in the upper right inset of Fig. 2. Also note that in this resonance-antiresonance-resonance trio, located in the vicinity of  $h\nu = 2|\eta|$ , the antiresonance becomes stronger in comparison with its predecessor antiresonance from the antiresonance-resonance pair shown in the vicinity of  $h\nu = 2|\eta|$  in Fig. 2 (see its upper right inset) in the regime of very small bias voltages,  $|eV| \ll \Gamma$ .

Our further results, presented in Fig. 4, show the differential quantum noise in the regime of large,  $|eV| \gtrsim \Gamma$ , and very large,  $|eV| \gg \Gamma$ , bias voltages. In this strongly nonequilibrium regime the differential noise vanishes at all frequencies except for vicinities of a few characteristic frequencies. First, the antiresonance located at  $h\nu = |eV|/2$  in Figs. 2 and 3 is fully washed out in strong nonequilibrium. Instead, at  $h\nu = |eV|/2$  there develops a resonance shown in the upper inset for  $V = V_1$  (black curve) and  $V = V_2$  (red curve). The universal (independent of  $\epsilon_d$ ) maximum of this resonance is equal to  $e^2/2$  while its full width at half of the maximum is equal to  $\Gamma$  as demonstrated in the upper inset. Further, in the vicinity of  $h\nu = 2|\eta|$  there develops an antiresonance-resonance pair shown in the lower inset. This antiresonance-resonance pair is independent of the bias voltage  $V$  for  $|eV| > \Gamma$ . Finally, at frequencies  $h\nu = 2|\eta| \mp |eV|/2$  there develop two resonances. The universal (independent of  $\epsilon_d$ ) maximum of these resonances is equal to  $e^2$  while their full width at half of the maximum is equal to  $\Gamma/2$  as demonstrated in the lower inset for  $V = V_1$  (black curve) and  $V = V_2$  (red curve).

The universal Majorana properties of finite frequency quantum noise presented above may intuitively be explained as follows.

First of all, from Eq. (23) one obtains the spectral function  $\nu(\epsilon) \equiv (-1/\pi\hbar)\text{Im}[\mathcal{G}_{hp}^R(\epsilon)]$ . The spectral function provides the quasiparticle spectrum of the quantum dot. It is easy to find from  $\nu(\epsilon)$  that for  $\xi = 0$  the quasiparticle spectrum of the quantum dot consists of three peaks located at  $\epsilon = 0, \mp 2|\eta|$ . These peaks have the same maximum equal to  $1/(\pi\Gamma)$ . The full width of the peak at  $\epsilon = 0$  is equal to  $\Gamma$  at half of its maximum. The full width of the peaks at  $\epsilon = \mp 2|\eta|$  is equal to  $\Gamma/2$  at half of the maximum. Moreover, for  $\xi \neq 0$  there appears a dip located near  $\epsilon = 0$ . For  $\epsilon_d \geq \Gamma$  the minimum of this dip vanishes as  $\nu(\epsilon) \sim \Gamma/(5\pi\epsilon_d^2)$ . This dip is extremely narrow for small  $\xi$  and large  $\eta$ . Its full width at half of its minimum is proportional to  $[(\epsilon_d\xi/\eta)^2]/\Gamma$ .

Now, having in mind the above structure of the spectral function, it is obvious from the energy conservation that photon absorption leading to the excitation of the quantum dot by energy  $\Delta\epsilon = 2|\eta|$  is responsible for the antiresonance-resonance pair (see Fig. 2) located at  $h\nu = 2|\eta|$  and for the two resonances (see Fig. 4) located at  $h\nu = 2|\eta| \mp |eV|/2$ . The latter two resonances also involve tunneling processes after which the quasiparticle energy in the final state is decreased (increased) by  $\Delta\epsilon_{qp} = |eV|/2$ , *i.e.* tunneling processes *topological superconductor (left contact) → quantum dot → left contact (topological superconductor)*. Likewise, the energy conservation admits photon absorption with weak excitations of the quantum dot, that is with excitation energies  $\Delta\epsilon \lesssim \Gamma$ , but involve tunneling processes after which the quasiparticle energy in the final state is increased by  $\Delta\epsilon_{qp} = |eV|/2$ , *left contact → quantum dot → topological superconductor*. Such processes are responsible for the formation of the antiresonance ( $|eV| < \Gamma$ ) or resonance

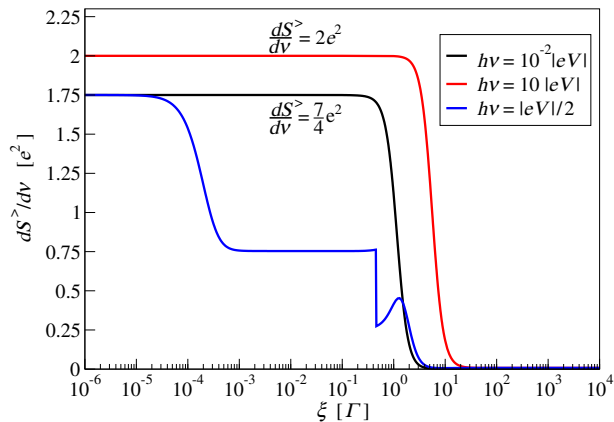


FIG. 5. The differential quantum noise  $\partial S^>(\nu, V)/\partial \nu$  as a function of the overlap energy  $\xi$  is shown for  $|eV|/\Gamma = 10^{-4}$ . Here, as in Fig. 2,  $k_B T/\Gamma = 10^{-12}$ ,  $\epsilon_d/\Gamma = 8.0$ ,  $|\eta|/\Gamma = 10^3$ . The black curve corresponds to  $h\nu/\Gamma = 10^{-6}$ , *i.e.* to the case  $h\nu < |eV|$ . The red curve corresponds to  $h\nu/\Gamma = 10^{-3}$ , *i.e.* to the case  $\Gamma > h\nu > |eV|$ . The blue curve corresponds to  $h\nu/\Gamma = 5 \cdot 10^{-5}$ , *i.e.* to the case  $h\nu = |eV|/2$  and, therefore, describes the behavior of the antiresonance minimum.

( $|eV| \gg \Gamma$ ) at  $h\nu = |eV|/2$ . Here, the above discussed dip in the spectral function near  $\epsilon = 0$  is detected at small bias voltages and temperatures leading to the antiresonance (see Fig. 2) in the differential noise at  $h\nu = |eV|/2$ . However, for large bias voltages this extremely narrow dip in the spectral function is not any more detected and thus effectively one has the situation where  $\xi = 0$ . Therefore, the resonance of the spectral function located around  $\epsilon = 0$  leads instead of the antiresonance to the resonance (see Fig. 4) in the differential noise at  $h\nu = |eV|/2$ . The full width of this resonance at half of its maximum is equal to  $\Gamma$ . This exactly corresponds to the full width of the spectral function peak at half of its maximum which is located at  $\epsilon = 0$  in the case  $\xi = 0$ . Finally, when  $|eV| \ll \Gamma$ , there is photon absorption with weak excitations of the quantum dot, that is with excitation energies  $\Delta\epsilon \lesssim \Gamma$ , and involves tunneling processes after which the quasiparticle energy in the final state is increased by  $\Delta\epsilon_{qp} \lesssim \Gamma$ . The first type of such tunneling includes tunneling processes *left contact*  $\rightarrow$  *quantum dot*  $\rightarrow$  *left contact* which are involved in photon absorption at frequencies  $h\nu < |eV|$  leading to the formation of the first low-energy plateau,  $\partial S^>(\nu, V)/\partial \nu = 7e^2/4$ , shown in Fig. 2. The second type of such tunneling includes tunneling processes *left contact*  $\rightarrow$  *quantum dot*  $\rightarrow$  *right contact* which are involved in photon absorption at frequencies  $h\nu > |eV|$ . Tunneling processes of the second type add to the tunneling processes of the first type, which are present also for  $h\nu > |eV|$ , and lead to the increase of the differential noise up to the second low-energy plateau,  $\partial S^>(\nu, V)/\partial \nu = 2e^2$ , shown in Fig. 2. As we have seen in Fig. 2, indeed, at  $h\nu = |eV|$  there is a jump in  $\partial S^>(\nu, V)/\partial \nu$ . Why the two low-energy plateaus are equal to exactly  $7e^2/4$  and  $2e^2$  is, however,

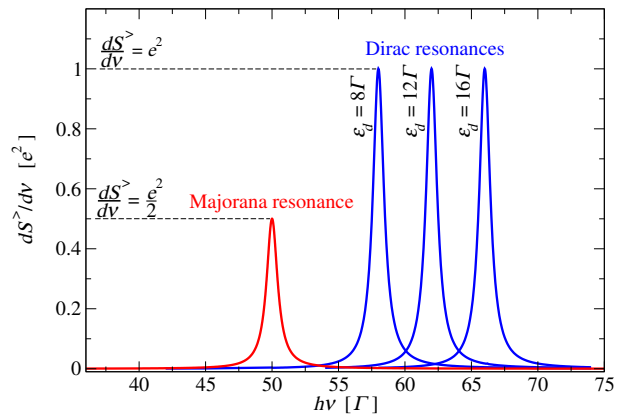


FIG. 6. The differential quantum noise  $\partial S^>(\nu, V)/\partial \nu$  as a function of the frequency  $\nu$  is shown for  $|eV|/\Gamma = 100.0$ . Here, as in Fig. 2,  $k_B T/\Gamma = 10^{-12}$ ,  $|\eta|/\Gamma = 10^3$ . The red curve is for the case of the well separated Majorana modes,  $\xi/\Gamma = 10^{-4}$ . In this case the Majorana resonance at  $h\nu = |eV|/2$  is universal, *i.e.* it is independent of  $\epsilon_d$  controlled by a gate voltage. The blue curves are for the case of strongly,  $\xi/\Gamma = 10^6$ , overlapping Majorana modes merging into a single Dirac fermion. In this case the Dirac resonance is not universal. Its location depends on  $\epsilon_d$  as  $\epsilon_d + |eV|/2$ . The three Dirac resonances are shown for  $\epsilon_d/\Gamma = 8, 12, 16$  from left to right, respectively.

an open question representing a challenge for future research elaborating more analytical approaches.

It is important to look at what will happen with the above discussed universal Majorana features of finite frequency noise if the Majorana bound states are absent. To this end we consider the scenario when the two Majorana bound states disappear via their significant overlap resulting in appearance of a single Dirac fermion instead of the unpaired Majoranas. Physically this is relevant for short topological superconductors. This situation can be modeled via increasing the overlap energy  $\xi$ . Different universal Majorana features shown above disappear in different ways which we demonstrate below.

As shown in Fig. 5, in the case  $|eV| \ll \Gamma$  the two low-frequency plateaus (see Fig. 2) with the universal values  $\partial S^>(\nu, V)/\partial \nu = 7e^2/4$  (black curve) for  $h\nu < |eV|$  and  $\partial S^>(\nu, V)/\partial \nu = 2e^2$  (red curve) for  $h\nu > |eV|$  are totally ruined when the two Majorana bound states merge into a single Dirac fermion. The blue curve shows what happens with the antiresonance (see Fig. 2) located at  $h\nu = |eV|/2$ . As one can see, the antiresonance is also destroyed when the Majorana bound states strongly overlap. It is interesting to note that for the extremely well,  $\xi/\Gamma < 10^{-5}$ , separated Majorana bound states the antiresonance fully disappears. But for a stronger overlap, such that all other universal Majorana features discussed above do not change, it can already be observed as is the case in Fig. 2 where  $\xi/\Gamma = 10^{-4}$ .

In Fig. 6 we demonstrate what happens with the Majorana resonance  $\partial S^>(\nu, V)/\partial \nu = e^2/2$  located at  $h\nu = |eV|/2$  for  $|eV| \gg \Gamma$ . When the two Majorana bound

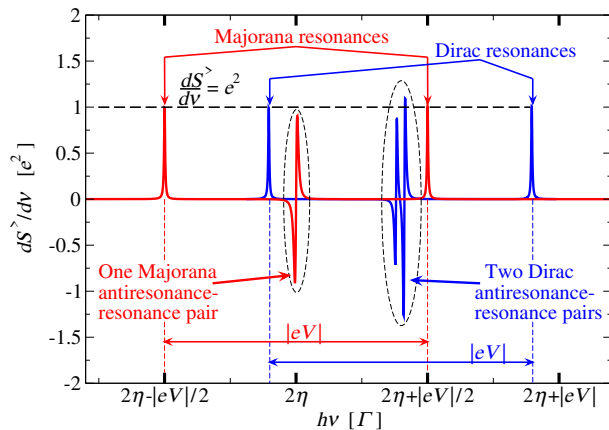


FIG. 7. The differential quantum noise  $\partial S^>(\nu, V)/\partial \nu$  as a function of the frequency  $\nu$  is shown for  $|eV|/\Gamma = 100.0$ . Here, as in Fig. 2,  $k_B T/\Gamma = 10^{-12}$ ,  $|\eta|/\Gamma = 10^3$ . The red curve is for the case of the well separated Majorana modes,  $\xi/\Gamma = 10^{-4}$ . The blue curve is for the case of significantly,  $\xi/\Gamma = 400$ , overlapping Majorana modes merging into a single Dirac fermion.

states strongly overlap and form a single Dirac fermion, instead of the Majorana resonance there develops a Dirac resonance which is twice stronger,  $\partial S^>(\nu, V)/\partial \nu = e^2$ . While the Majorana resonance is universal, that is independent of  $\epsilon_d$ , the Dirac resonance is not universal because its location is specified by  $\epsilon_d$  as  $\epsilon_d + |eV|/2$ . Therefore, if in an experiment one continuously changes the gate voltage controlling  $\epsilon_d$ , this Dirac resonance will continuously flow according to that change as shown in Fig. 6 for three different values of  $\epsilon_d$ .

Finally, Fig. 7 illustrates for  $|eV| \gg \Gamma$  how the two universal (*i.e.* independent of  $\epsilon_d$ ) Majorana resonances (red curve)  $\partial S^>(\nu, V)/\partial \nu = e^2$  located at  $h\nu = 2|\eta| \mp |eV|/2$  turn into two Dirac resonances (blue curve). These Dirac resonances have the same magnitude  $e^2$  as the Majorana resonances but they are shifted from the points  $2|\eta| \mp |eV|/2$ . This shift depends on  $\xi$  but the distance between the Dirac resonances remains equal to  $|eV|$ . For larger values of  $\xi$  the Dirac resonances will shift to higher frequencies,  $h\nu \gg 2|\eta| \mp |eV|/2$ . Moreover, as we have seen in Fig. 4, there is one (odd number) universal Majorana antiresonance-resonance pair centered at  $2|\eta|$  as shown in Fig. 7 by the dashed ellipse around the red curve. However, when the two Majorana bound states significantly overlap and form a single Dirac fermion, there develop two (even number) Dirac antiresonance-resonance pairs located just in the center between the two Dirac resonances as it is shown in Fig. 7 by the dashed ellipse around the blue curve.

#### IV. CONCLUSION

In conclusion, we have explored the photon absorption spectra governed by Majorana zero modes in a meso-

scopic setup and predicted their universal nature revealed via our extensive numerical computations of the differential quantum noise over a large range of frequencies and bias voltages. Although finite frequency noise in specific settings, *e.g.*, in a topological superconductor-normal metal structure [26, 27], may be used as a tool to distinguish between Majorana zero modes and zero-energy ordinary Andreev bound states, universal fingerprints of the Majorana finite frequency quantum noise have never been discussed. At the same time universality of finite frequency quantum noise is of particular relevance for experiments on Majorana zero modes and their applications. Our setup is especially attractive for state-of-the-art experiments involving quantum noise detectors able to reach the quantum limit and separately access photon absorption and emission spectra. One reason is that single-electron transistors and noninteracting resonant-level quantum noise detectors, where only one energy level contributes to transport (and thus Coulomb-blockade effects may be neglected), have already been proposed [29–31]. Importantly, these mesoscopic quantum noise detectors are able to reach the quantum limit in nonequilibrium states induced by both small and large bias voltages. Another reason is that our results for quantum dot setups, where only one energy level contributes to transport, should be robust against disorder. Indeed, disorder might affect the Majorana transport through the quantum dot in two ways. First, the topological superconductor itself can be disordered and interplay between topology and disorder specifies when the Majorana bound states are present or absent at the ends of the topological superconductor. In this case the finite frequency noise will follow that interplay between topology and disorder and our results presented here will show either universal Majorana or nonuniversal Dirac behavior depending on whether the Majorana bound states are, respectively, present or absent at the ends of the topological superconductor. Here, for a typical setup, we neglect a feedback of a small quantum dot on a large topological superconductor. Otherwise, if such a feedback becomes significant, there will appear a complicated interplay between topology and disorder of the topological superconductor and nonequilibrium states of the quantum dot. This complicated nonequilibrium dynamics involving topology and disorder would be a challenge for future research. Second, there can be a particular realization of disorder in the quantum dot whose discrete energy spectrum is specified by that particular disorder. In this case one may use the gate voltage to tune the chemical potential around a single-particle energy level  $\epsilon_d$  to reach the transport regime where only one energy level  $\epsilon_d$  essentially contributes to transport as discussed above. Then our results on finite frequency noise will be applicable again. This assumes that for a particular realization of disorder the distances between the energy levels of the quantum dot should be large enough because otherwise more than one energy level will contribute to transport. Such a multilevel regime would be another

challenge for future research.

Both of the above discussed reasons imply that the results presented in this work pertain to realistic systems and thus they are of immediate interest for experiments on Majorana finite frequency noise in the quantum limit.

## ACKNOWLEDGMENTS

The author thanks Milena Grifoni, Andreas K. Hüttel and Wataru Izumida for invaluable discussions.

- 
- [1] A. Yu. Kitaev, “Unpaired Majorana fermions in quantum wires,” *Phys.-Usp.* **44**, 131 (2001).
- [2] E. Majorana, “Teoria simmetrica dell’elettrone e del positrone,” *Nuovo Cimento* **14**, 171 (1937).
- [3] J. Alicea, “New directions in the pursuit of Majorana fermions in solid state systems,” *Rep. Prog. Phys.* **75**, 076501 (2012).
- [4] M. Leijnse and K. Flensberg, “Introduction to topological superconductivity and Majorana fermions,” *Semicond. Sci. Technol.* **27**, 124003 (2012).
- [5] M. Sato and S. Fujimoto, “Majorana fermions and topology in superconductors,” *J. Phys. Soc. Japan* **85**, 072001 (2016).
- [6] R. M. Lutchyn, E. P. A. M. Bakkers, L. P. Kouwenhoven, P. Krogstrup, C. M. Marcus, and Y. Oreg, “Majorana zero modes in superconductor-semiconductor heterostructures,” *Nat. Rev. Mater.* **3**, 52 (2018).
- [7] V. Mourik, K. Zuo, S. M. Frolov, S. R. Plissard, E. P. A. M. Bakkers, and L. P. Kouwenhoven, “Signatures of Majorana fermions in hybrid superconductor-semiconductor nanowire devices,” *Science* **336**, 1003 (2012).
- [8] S. M. Albrecht, A. P. Higginbotham, M. Madsen, F. Kuemmeth, T. S. Jespersen, J. Nygård, P. Krogstrup, and C. M. Marcus, “Exponential protection of zero modes in Majorana islands,” *Nature* **531**, 206 (2016).
- [9] H. Zhang, C.-X. Liu, S. Gazibegovic, D. Xu, J. A. Logan, G. Wang, N. van Loo, J. D. S. Bommer, M. W. A. de Moor, D. Car, R. L. M. O. het Veld, P. J. van Veldhoven, S. Koelling, M. A. Verheijen, M. Pendharkar, D. J. Pennachio, B. Shojaei, J. S. Lee, C. J. Palmström, E. P. A. M. Bakkers, S. D. Sarma, and L. P. Kouwenhoven, “Quantized Majorana conductance,” *Nature* **556**, 74 (2018).
- [10] S. Smirnov, “Majorana tunneling entropy,” *Phys. Rev. B* **92**, 195312 (2015).
- [11] N. Hartman, C. Olsen, S. Lüscher, M. Samani, S. Fallahi, G. C. Gardner, M. Manfra, and J. Folk, “Direct entropy measurement in a mesoscopic quantum system,” *Nature Physics* **14**, 1083 (2018).
- [12] A. Yu. Kitaev, “Fault-tolerant quantum computation by anyons,” *Ann. Phys.* **303**, 2 (2003).
- [13] C. Nayak, S. H. Simon, A. Stern, M. Freedman, and S. Das Sarma, “Non-abelian anyons and topological quantum computation,” *Rev. Mod. Phys.* **80**, 1083 (2008).
- [14] J. Alicea, Y. Oreg, G. Refael, F. von Oppen, and M. P. A. Fisher, “Non-Abelian statistics and topological quantum information processing in 1D wire networks,” *Nature Physics* **7**, 412 (2011).
- [15] D. Aasen, M. Hell, R. V. Mishmash, A. Higginbotham, J. Danon, M. Leijnse, T. S. Jespersen, J. A. Folk, C. M. Marcus, K. Flensberg, and J. Alicea, “Milestones toward Majorana-based quantum computing,” *Phys. Rev. X* **6**, 031016 (2016).
- [16] S. Vijay and L. Fu, “Teleportation-based quantum information processing with Majorana zero modes,” *Phys. Rev. B* **94**, 235446 (2016).
- [17] F. L. Pedrocchi and D. P. DiVincenzo, “Majorana braiding with thermal noise,” *Phys. Rev. Lett.* **115**, 120402 (2015).
- [18] K. Gharavi, D. Hoving, and J. Baugh, “Readout of Majorana parity states using a quantum dot,” *Phys. Rev. B* **94**, 155417 (2016).
- [19] A. A. Clerk, M. H. Devoret, S. M. Girvin, F. Marquardt, and R. J. Schoelkopf, “Introduction to quantum noise, measurement, and amplification,” *Rev. Mod. Phys.* **82**, 1155 (2010).
- [20] D. E. Liu, M. Cheng, and R. M. Lutchyn, “Probing Majorana physics in quantum-dot shot-noise experiments,” *Phys. Rev. B* **91**, 081405(R) (2015).
- [21] D. E. Liu, A. Levchenko, and R. M. Lutchyn, “Majorana zero modes choose Euler numbers as revealed by full counting statistics,” *Phys. Rev. B* **92**, 205422 (2015).
- [22] C. W. J. Beenakker, “Random-matrix theory of Majorana fermions and topological superconductors,” *Rev. Mod. Phys.* **87**, 1037 (2015).
- [23] A. Haim, E. Berg, F. von Oppen, and Y. Oreg, “Current correlations in a Majorana beam splitter,” *Phys. Rev. B* **92**, 245112 (2015).
- [24] S. Smirnov, “Non-equilibrium Majorana fluctuations,” *New J. Phys.* **19**, 063020 (2017).
- [25] S. Smirnov, “Universal Majorana thermoelectric noise,” *Phys. Rev. B* **97**, 165434 (2018).
- [26] S. Valentini, M. Governale, R. Fazio, and F. Taddei, “Finite-frequency noise in a topological superconducting wire,” *Physica E* **75**, 15 (2016).
- [27] D. Bathellier, L. Raymond, T. Jonckheere, J. Rech, A. Zazunov, and T. Martin, “Finite frequency noise in a normal metal - topological superconductor junction,” *Phys. Rev. B* **99**, 104502 (2019).
- [28] A. Altland and B. Simons, *Condensed Matter Field Theory*, 2nd ed. (Cambridge University Press, Cambridge, 2010).
- [29] D. V. Averin, “Quantum computing and quantum measurement with mesoscopic Josephson junctions,” *Fortschr. Phys.* **48**, 1055 (2000).
- [30] A. A. Clerk and A. D. Stone, “Noise and measurement efficiency of a partially coherent mesoscopic detector,” *Phys. Rev. B* **69**, 245303 (2004).
- [31] D. Mozyrsky, I. Martin, and M. B. Hastings, “Quantum-limited sensitivity of single-electron-transistor-based displacement detectors,” *Phys. Rev. Lett.* **92**, 018303 (2004).